Renewable Energy 211 (2023) 809–821

Contents lists available at ScienceDirect

Renewable Energy

journal homepage: www.elsevier.com/locate/renene

Evaluation and future projections of wind energy resources over the Northern Hemisphere in CMIP5 and CMIP6 models

Haozeyu Miao [a,b,d], Haiming Xu [a,b], Gang Huang [c,d,e,*], Kai Yang [d,**]

[a] Key Laboratory of Meteorological Disaster/KLME/ILCEC/CIC-FEMD, Nanjing University of Information Science & Technology, Nanjing, 210044, China
[b] School of Atmospheric Sciences, Nanjing University of Information Science & Technology, Nanjing, 210044, China
[c] Laboratory for Regional Oceanography and Numerical Modeling, Qingdao National Laboratory for Marine Science and Technology, Qingdao, 266237, China
[d] State Key Laboratory of Numerical Modeling for Atmospheric Sciences and Geophysical Fluid Dynamics, Institute of Atmospheric Physics, Chinese Academy of Sciences, Beijing, 100029, China
[e] University of Chinese Academy of Sciences, Beijing, 100049, China

ARTICLE INFO

Keywords:
Wind energy resource
Greenhouse warming
The Northern Hemisphere
Climate model

ABSTRACT

Understanding how the wind energy resources will change in a future climate under different greenhouse gas (GHG) emission scenarios is critical for global energy safety and economy. In this study, we evaluate the simulated wind speed over the Northern Hemisphere in global climate models that participate in the Coupled Model Intercomparison Project Phase 5 (CMIP5) and Phase 6 (CMIP6) using observation, and further show the future change of wind speed and wind energy in the Northern Hemisphere under four different GHG emission scenarios using superior models. We find that the CMIP6 models are generally better in simulating surface wind speeds over the Northern Hemisphere than CMIP5 models, in terms of spatial pattern and long-term trend. For future projection of wind speed at the end of the 21st century, models generally show a continued decreasing trend, except in SSP3-7.0 scenario. The change in wind energy and emissions are non-linearly related in different regions, as wind speed exhibits the fastest drop over Europe and Asia while shows the flattest trend over North America under SSP3-7.0. Our results suggest that higher emission scenario will undermine the magnitude of the wind energy resources and more importantly, reshape its spatial distribution over the Northern Hemisphere.

1. Introduction

Renewable energy such as wind energy plays a crucial role in reaching the emission reduction goals set by various countries, and will provide 36% of global electricity supply by 2030 [1]. Wind energy has been widely used in commercial applications, providing the second largest installed renewable energy capacity in the world, which is of great significance to energy conservation and emission reduction [2]. According to the Global Wind Report 2021 released by the Global Wind Energy Council (GWEC) [3], 86.9 GW of wind capacity was added on land globally in 2020, leading cumulative onshore wind energy installed capacity beyond the 700 GW milestone. Countries in the Northern Hemisphere such as China contributes the most newly installed capacity with 48.9 GW, accounting for 56.3% of global new installations. The US ranked second with 19.4%, nearly 17 GW.

Wind power density, representing the intensity of wind energy, varies with the cube of wind speed [4]. Small fluctuations in wind speed can result in significant changes in wind power density. During the recent decades, wind speeds have decreased considerably over many areas on land such as the US, Canada, China, and Spain, which has led to conspicuous reductions in wind energy resources [5–10]. Wind energy is susceptible to the effects of climate change, since wind power can only be generated under stable wind flow conditions. However, climate change has been suggested to have an important influence on the geographical distribution, intra-annual and inter-annual variability of wind resources in certain regions, affecting the design and operation of wind turbines and posing a significant threat to power supply in those areas [11]. Onshore wind turbines typically have a lifetime of about 20

* Corresponding author. State Key Laboratory of Numerical Modeling for Atmospheric Sciences and Geophysical Fluid Dynamics, Institute of Atmospheric Physics, Chinese Academy of Sciences, Beijing, 100029, China.
** Corresponding author. State Key Laboratory of Numerical Modeling for Atmospheric Sciences and Geophysical Fluid Dynamics, Institute of Atmospheric Physics, Chinese Academy of Sciences, Beijing, 100029, China.
E-mail addresses: hg@mail.iap.ac.cn (G. Huang), yangkai@mail.iap.ac.cn (K. Yang).

https://doi.org/10.1016/j.renene.2023.05.007
Received 18 March 2022; Received in revised form 7 March 2023; Accepted 1 May 2023
Available online 6 May 2023

years, so an assessment of how wind resources will change over the next few decades under global warming scenarios is critical.

Global climate models (GCMs), such as these involved in the Coupled Model Intercomparison Project Phase 5 (CMIP5) [12] coordinated by the World Climate Research Programme's (WCRP) Working Group on Coupled Modeling (WGCM), have been widely used as a main tool to study future changes of wind energy resources [13–18]. However, the GCMs in CMIP5 have been suggested to have limited capability in simulating the spatiotemporal characteristics of wind speed, such as reproducing the historical decline of surface wind speed over the Northern Hemisphere [5]. Recently, a new generation of GCMs participating in the sixth phase of the CMIP (CMIP6) becomes available [19]. Compared with the CMIP5 models, the CMIP6 models have generally higher resolutions, more consistent responses to aerosols, more short-term forcing factors and surficial processes, and also more advanced reconstruction of external conditions [20]. Krishnan et al. [21] compared the performances of CMIP5 and CMIP6 GCMs in simulating near-surface wind speed over the Bay of Bengal (BoB), and found that the CMIP6 models have a generally better performance in simulating the magnitude and variability than the CMIP5 models. Oudar found that the present-day zonal wind biases in the CMIP6 models over the Northern Hemisphere mid-latitude atmospheric circulation are reduced compared to those in the CMIP5 models [22].

To achieve the Paris Agreement, which aims to limit the global warming below 1.5 °C and well below 2 °C, the greenhouse gas (GHG) emission has to decline in the near future. While the wind power can be the cornerstone of the GHG emission reduction and green recovery, climate changes associated with different emission scenarios can in turn influence the spatial distribution and intensity of wind energy. Under a low-emission scenario, the wind speed change may be different from that under a high-emission scenario [23,24]. The CMIP6 models provide future projections of global wind speed under shared socio-economic paths (SSPs) from SSP1-SSP5 that are driven by different anthropogenic emissions and land use scenarios, giving us an opportunity to discuss the possible future change of global wind speed or wind energy change under the influence of different climate change conditions or climate policies [25,26]. Current studies [27–29] mainly focus on the impact of high and low emission scenarios on wind energy, overlooking an peculiar scenario, SSP3-7.0, which represents the highest aerosol emissions of all scenarios and may have severe impacts on wind energy [30].

Till now, an overall comparison of wind speed in CMIP5 and CMIP6 models over the three major wind power markets in the Northern Hemisphere including Europe, Asia, and North America under difference emission scenarios, especially the SSP3-7.0, have not been carried out. The aim of this study is to perform a comprehensive assessment of surface wind speed over the Northern Hemisphere based on the intercomparison between CMIP5 and CMIP6 GCMs, and then apply selected GCMs for detailed historical assessment and future projection of wind speed and wind power density. The framework of this paper is summarized as follows. In section 2, we introduce the observational and model datasets and methods used in this study. The results of the intercomparison between CMIP5 and CMIP6 GCMs are presented in section 3. In sections 4 and 5, we give detailed evaluation and future projection, respectively, based on the superior GCMs. In section 6, we discuss results of this study, followed by conclusions in section 7.

2. Data and methods

2.1. Data

2.1.1. Observational data

Two sets of observed surface wind speed data are used in this study. The first is the Integrated Surface Database (ISD) [31] originated in 1998 from the National Centers for Environmental Information (NCEI) of the National Oceanic and Atmospheric Administration (NOAA), which provides hourly global surface data including wind speed at more than 11,000 active stations. The other is the Daily Climate Data (V3.0) from the China Meteorological Data Service Center (CMDC) of the Chinese Meteorological Administration's (CMA), which provides daily data from 824 Chinese surface stations. Quality control (QC), including validity checks, extreme value checks, internal and external continuity checks, and manual verification and correction is conducted to ensure the quality of wind speed time series. The QC algorithms are designed to eliminate obvious errors in the data, ensuring that valid values are not removed or marked as errors to minimize data overflow [31]. The procedures are as follows. First, removing sites with a distant move, only retaining sites with less than 0.02°(approximately 2 km) in horizontal relocation and less than 20 m in vertical relocation. Then, removing stations with large gaps and keeping stations with more than 360 days of records in a year. Finally, inhomogeneous records are removed, and records that passed all QC checks of ISD are kept [5,32]. After QC, 10-m surface wind speeds at 1038 stations are retained, among which 687 stations are from the NECI ISD and 351 stations are from the CMDC daily surface observation V3.0, from 1979 to 2014. Specifically, there are 224, 531, and 215 stations in Europe, Asia, and North America, respectively. In addition, to verify the reliability of the observational data, we use another observed wind speed dataset generated based on Global Summary of Day (GSOD) database following strict QC procedures [33], and attain similar results.

2.1.2. Model outputs

The CMIP5 historical simulations provide surface wind speed field from 1850 to 2005. As an updated version, the CMIP6 historical simulations extend the period to 2014. Here, we use 29 CMIP5 models (Table 1) and 42 CMIP6 models (Table 2). Monthly surface wind speed data are extracted for historical assessment, for the time periods of 1979–2005 in the CMIP5 models and of 1979–2014 in the CMIP6 models. For future projections, 23 CMIP6 GCMs containing four typical SSPs are extracted, which are also listed in Table 2. The four typical emission scenarios are chosen to compare the changes of future wind speed and wind energy, including SSP1-2.6, SSP2-4.5, SSP3-7.0, and SSP5-8.5. SSP1-2.6 represents a low radiative forcing scenario, with

Table 1
Information about various CMIP5 models used for the study.

Institution/Nation	Model name	Spatial resolution (in °)
CAS/China	FGOALS-s2	2.8125 × 1.6667
CMCC/Italy	CMCC-CESM	3.75 × 3.75
	CMCC-CM	0.75 × 0.75
	CMCC-CMS	1.875 × 1.875
CNRM-CERFACS/France	CNRM-CM5	1.40625 × 1.40625
	CNRM-CM5-2	1.40625 × 1.40625
CSIRO/Australia	ACCESS1.0	1.875 × 1.25
	ACCESS1.3	1.875 × 1.25
	CSIRO-Mk3.6.0	1.875 × 1.875
INM/Russia	INMCM4	2 × 1.5
MIROC/Japan	MIROC4h	0.5625 × 0.5625
	MIROC5	1.40625 × 1.40625
	MIROC-ESM	2.8125 × 2.8125
	MIROC-ESM-CHEM	2.8125 × 2.8125
MOHC/UK	HadCM3	3.75 × 2.5
	HadGEM2-AO	1.875 × 1.25
	HadGEM2-CC	1.875 × 1.25
	HadGEM2-ES	1.875 × 1.25
MPI/Germany	MPI-ESM-LR	1.875 × 1.875
	MPI-ESM-MR	1.875 × 1.875
	MPI-ESM-P	1.875 × 1.875
MRI/Japan	MRI-CGCM3	1.125 × 1.125
	MRI-ESM1	1.125 × 1.125
NASA-GISS/USA	GISS-E2-H	2.5 × 2
	GISS-E2-H-CC	2.5 × 2
	GISS-E2-R	2.5 × 2
	GISS-E2-R-CC	2.5 × 2
NOAA-GFDL/USA	GFDL-ESM2G	2.5 × 2
	GFDL-ESM2M	2.5 × 2

Table 2
Information about various CMIP6 models used for the study (The models marked with "*" are used for future projections).

Institution/Nation	Model name	Spatial resolution (in °)
AS-RCEC/China	TaiESM1*	1.25 × 0.9375
AWI/Germany	AWI-CM-1-1-MR*	0.9375 × 0.9375
	AWI-ESM-1-1-LR	1.875 × 1.875
BCC/China	BCC-CSM2-MR*	1.125 × 1.125
	BCC-ESM1	2.8125 × 2.8125
CAMS/China	CAMS-CSM1-0*	1.125 × 1.125
CAS/China	CAS-ESM2-0*	1.40625 × 1.40625
	FGOALS-f3-L*	1.25 × 1
	FGOALS-g3*	2 × 2.25
CCCMA/Canada	CanESM5*	2.8125 × 2.8125
CMCC/Italy	CMCC-CM2-SR5*	1.25 × 0.9375
CSIRO/Australia	ACCESS-CM2*	1.875 × 1.25
	ACCESS-ESM1-5*	1.875 × 1.25
EC-Earth/Europe	EC-Earth3*	0.703125 × 0.703125
	EC-Earth3-AerChem	0.703125 × 0.703125
	EC-Earth3-Veg*	0.703125 × 0.703125
	EC-Earth3-Veg-LR	1.125 × 1.125
E3SM/USA	E3SM-1-0	1 × 1
	E3SM-1-1	1 × 1
	E3SM-1-1-ECA	1 × 1
FIO-QLNM/China	FIO-ESM-2-0	1.25 × 0.9375
INM/Russia	INM-CM4-8*	2 × 1.5
	INM-CM5-0*	2 × 1.5
IPSL/France	IPSL-CM6A-LR	2.5 × 1.25874
KIOST/Korea	KIOST-ESM	1.875 × 1.875
MIROC/Japan	MIROC6*	1.40625 × 1.40625
MPI/Germany	MPI-ESM-1-2-HAM	1.875 × 1.875
	MPI-ESM1-2-HR*	0.9375 × 0.9375
	MPI-ESM1-2-LR*	1.875 × 1.875
NASA-GISS/USA	GISS-E2-1-G	2.5 × 2
	GISS-E2-1-G-CC	2.5 × 2
	GISS-E2-1-H	2.5 × 2
	GISS-E2-2-H	2.5 × 2
NCAR/USA	CESM2	1.25 × 0.9375
	CESM2-FV2	2.5 × 1.875
	CESM2-WACCM*	1.25 × 0.9375
	CESM2-WACCM-FV2	2.5 × 1.875
NCC/Norway	NorESM2-LM*	2.5 × 1.875
	NorESM2-MM*	1.25 × 0.9375
NIMS-KMA/Korea	KACE-1-0-G*	1.875 × 1.25
NOAA-GFDL/USA	GFDL-ESM4*	1.25 × 1
SNU/Korea	SAM0-UNICON	1.25 × 0.9375

radiative forcing stabilizing at about 2.6 Wm^{-2} in 2100. In this scenario, the global average temperature would be significantly lower than 2 °C relative to the pre-industrial revolution multi-model ensemble (MME) average. The moderate radiative forcing scenario of SSP2-4.5 will stabilize at about 4.5 Wm^{-2} in 2100. The land use and aerosol pathways are not extreme, and represent only a combination of a moderate social vulnerability and moderate radiative forcing scenario. The medium-high radiative forcing scenario of SSP3-7.0 stabilizes at about 7.0 Wm^{-2} in 2100. This pathway represents a medium-large amount of land use change (especially global forest cover decline) and high climate forcing factors (especially SO_2). SSP5-8.5 signifies a high radiative forcing scenario, with a pathway to high emissions of 8.5 Wm^{-2} by 2100. This scenario delays action on climate and environmental protection, and achieves strong economic growth through fossil fuel emissions. All model outputs are converted to 1° × 1° grid using bilinear interpolation [34] in order to facilitate comparison.

2.2. Methods

2.2.1. Temporal and spatial descriptions

In this study, the research area in the Northern Hemisphere covers 130°W-150°E, 0°-72°N of which the ranges of latitude and longitude of three regions considered are (30°-72°N, 20°W-50°E) for Europe, (0°-55°N, 50°-150°E) for Asia, and (20°-55°N, 60°-140°W) for North America. The spatial distribution maps are based on an interpolation of observational sites to 1° × 1° grid using Cressman objective analysis [35]; countries and regions with few sites are not selected. Cressman used a stepwise revision approach to perform an iterative improvement type objective analysis using an input triplet set. Multiple passes of descending radii of influence are used for each gridpoint to obtain better estimates. Other assessments like bar, line, and Taylor diagram use an interpolation of gridded data to observational sites.

The evaluation is based on annual, seasonal, and monthly scales. The season is defined as spring (March–May; MAM), summer (June–August; JJA), autumn (September–November; SON), and winter (December–February; DJF).

2.2.2. Evaluation of individual model and the multi-model ensemble (MME)

The Taylor diagram comprehensively considers the three statistics of root mean square difference, standard deviation ratio, and pattern correlation coefficient with respect to the observations. It is often used to judge the performance of individual models [36].

First, the pattern correlation coefficient (R) is a quantitative indicator of the correlation of the model and is calculated as follows:

$$R = \frac{\frac{1}{N}\sum_{n=1}^{N}(m_n - \overline{m})(o_n - \overline{o})}{\sigma_m \sigma_o} \tag{1}$$

The second metric is the centered root mean squared difference (E):

$$E = \left\{ \frac{1}{N}\sum_{n=1}^{N}\left[(m_n - \overline{m}) - (o_n - \overline{o})\right]^2 \right\}^{1/2} \tag{2}$$

The third indicator is the standard deviation ratio between the model and the reference value. The standard deviation and the ratio are calculated, respectively, as follows:

$$\sigma_A = \left[\frac{1}{N}\sum_{n=1}^{N}(A_n - \overline{A})^2 \right]^{1/2} \tag{3}$$

$$ratio = \sigma_m / \sigma_o \tag{4}$$

The cosine relationship of the three indicators is:

$$E^2 = ratio^2 + ref^2 - 2ratio \times ref \times R \tag{5}$$

where the value of *ref* is 1.

In the above equations, m_n and o_n are the wind speed time series of the model and observations. and $\overline{o}$ are the average values of the model and the observed data. σ_o is the observed standard deviation, and σ_m is the model standard deviation. *An* and $\overline{A}$ are the wind speed time series and the average value, respectively. N is the corresponding sample size. N is the corresponding sample size.

In addition, the MMEs for the CMIP6 models are established for the future projection of wind speed and wind power density at the end of the 21st century. MMEs will generally give more reliable results than individual models.

2.2.3. Changes in wind speed and wind power density

Linear trends in wind speed for individual models as well as for their MMEs are calculated using the least-square method. Wind power density (*WPD*; units: Wm^{-2}) is the kinetic energy of air flow passing vertically through the unit cross-sectional area in unit time, and is defined as follows [32]:

$$WPD = \frac{1}{2}\rho U^3 \tag{6}$$

where ρ is air density (units: kgm^{-3}; a value of 1.225 kgm^{-3} is assumed) and U is wind speed (units: ms^{-1}).

The typical height of a modern commercial wind turbine is about 80

m, while surface wind speeds are measured around 10 m. So, surface wind speeds from the observations and model outputs are extrapolated to 80 m using the empirical power law [37]:

$$\frac{u_2}{u_1} = \left(\frac{z_2}{z_1}\right)^{\alpha} \tag{7}$$

where u_2 and u_1 denote the wind speeds at heights z_2 and z_1, respectively. The power law index α is approximately 0.14 under neutral stability condition, as widely used in wind energy climatology studies [38–40].

Percentage change in wind power density under different SSP scenarios for the future period (2050–2099) are calculated as the respective change from the historical period (1965–2014), which is defined by:

$$Futurechange = \left(Mean_{future} - Mean_{historical}\right)/Mean_{historical} \times 100 \tag{8}$$

3. Comparison of CMIP5 and CMIP6 models with the observations

The spatial maps of differences of the annual, JJA, and DJF mean surface wind speed of CMIP5 MME and CMIP6 MME with respect to the observations is presented in Fig. 1. Results indicate that the GCMs generally underestimate surface wind speeds in the US, western Europe, northern India, and Southeast Asia. The CMIP6 models have smaller differences compared to the CMIP5 models, narrowing from approximately −1.5 ms^{-1} to −1.0 ms^{-1} in these regions (Fig. 1a and b). The negative deviation in the US and Europe appears mainly in summer, especially in the CMIP5 where the value can be up to −2.0 ms^{-1} on average, while the value in the CMIP6 is about −1.5 ms^{-1} (Fig. 1c and d). In winter, these negative biases are significantly improved, especially in the CMIP6, where the bias is only in the range of −0.5 ms^{-1} to 0.5 ms^{-1} in most of the US (Fig. 1e and f).

Conversely, the surface wind speed in western and northern China in all periods is overestimated in the GCMs (Fig. 1 b, d, and f). This may be due to the coarse spatial resolution of the GCMs and the complex topography of these regions, such as the Qinghai-Tibet Plateau. For regions with complex terrain, surface conditions such as topographic relief, sea-land interface, or uneven distributions of precipitation and clouds may cause changes in the medium- and small-scale atmospheric motion, and the influence of topography is critical for wind field simulation in such cases, especially for near-surface wind speed [41].

Focusing on individual models, overall speaking, the simulated results of the individual CMIP6 models are relatively similar, while the results of the individual CMIP5 models are less closer, with large differences among CMIP5 models (Fig. 2). In the CMIP5 GCMs, the standard deviation ratio is in the range of 0.73–1.30, the correlation coefficient is between 0.16 and 0.59, and the root mean square difference range is 0.89–1.40. These values have been substantially improved in the CMIP6, with the standard deviation ratio tightening to 0.75–1.12, the correlation coefficient rising to 0.39–0.71, and the root mean square difference reducing to 0.73–1.12. In agreement with Carvalho's [16] results, using the CMIP5 models, the large uncertainty of the simulations is mainly due to the low model resolution, which makes it difficult to describe steep terrain in detail, while the enhancement of the CMIP6 models in resolution makes the simulations remarkably more consistent. The standard deviation ratio, correlation coefficient, and root mean square difference of the MMEs are 1.04, 0.48, and 1.04 in the CMIP5; and they are 0.96, 0.56, and 0.92 in the CMIP6, respectively, indicating considerable improvements from the CMIP5 to CMIP6. In particular, CESM2, CESM2-WACCM, NorESM2-LM, and NorESM2-MM are more reliable models, while BCC-CSM2-MR, BCC-ESM1, FGOALS-f3-L, and FGOALS-g3 are poor performing models based on the three statistics.

Fig. 3 shows the annual trends of wind speed anomaly in individual CMIP5 and CMIP6 GCMs, their MMEs, and the observations. The observed data exhibit a notable reduction over time, with the surface wind speed dropping by 0.26 ms^{-1} during 1979–2005 and by 0.34 ms^{-1} during 1979–2014 altogether. There are apparent inconsistencies among individual CMIP5 GCMs; and nearly half of the models show increasing trends, and the other half show decreasing trends, with the largest differences occurring between MIROC5 and MRI-CGCM3. MIROC5 has the best

performance, with the trend magnitude closest to the observed data.

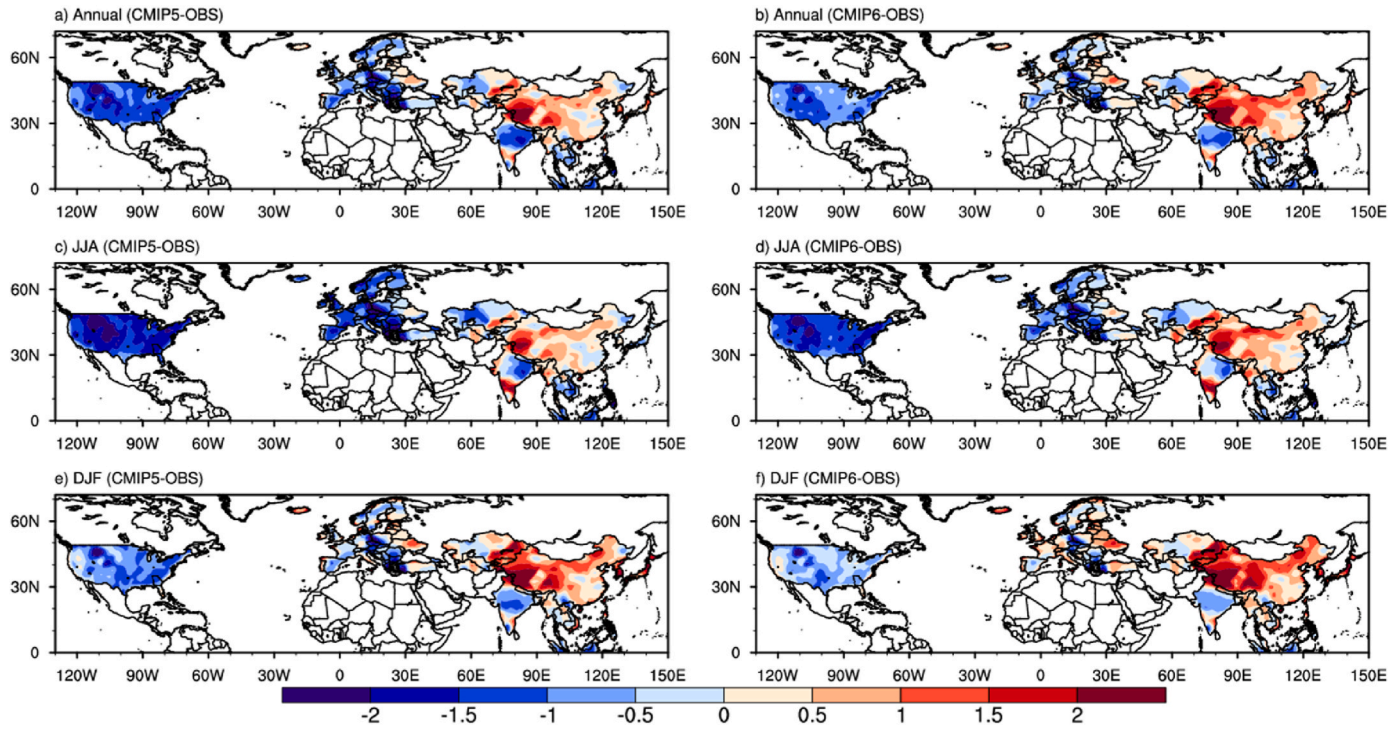

Fig. 1. Annual (a and b), JJA (c and d) and DJF (e and f) mean surface wind speed biases (ms^{-1}) between the observational data and CMIP5 (a, c and e) during 1979–2005, and CMIP6 (b, d and f) during 1979–2014.

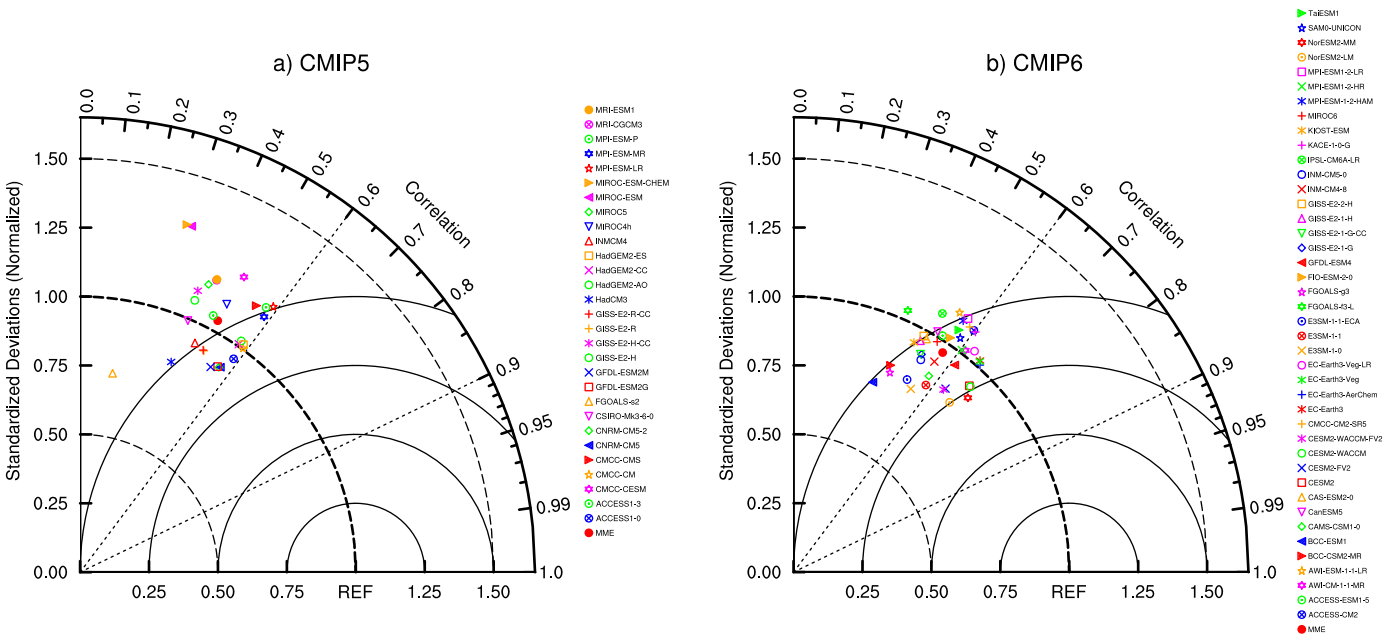

Fig. 2. Taylor diagrams of surface wind speed (ms^{-1}) over the Northern Hemisphere for (a) CMIP5 GCMs and (b) CMIP6 GCMs, together with their MMEs for the historical period.

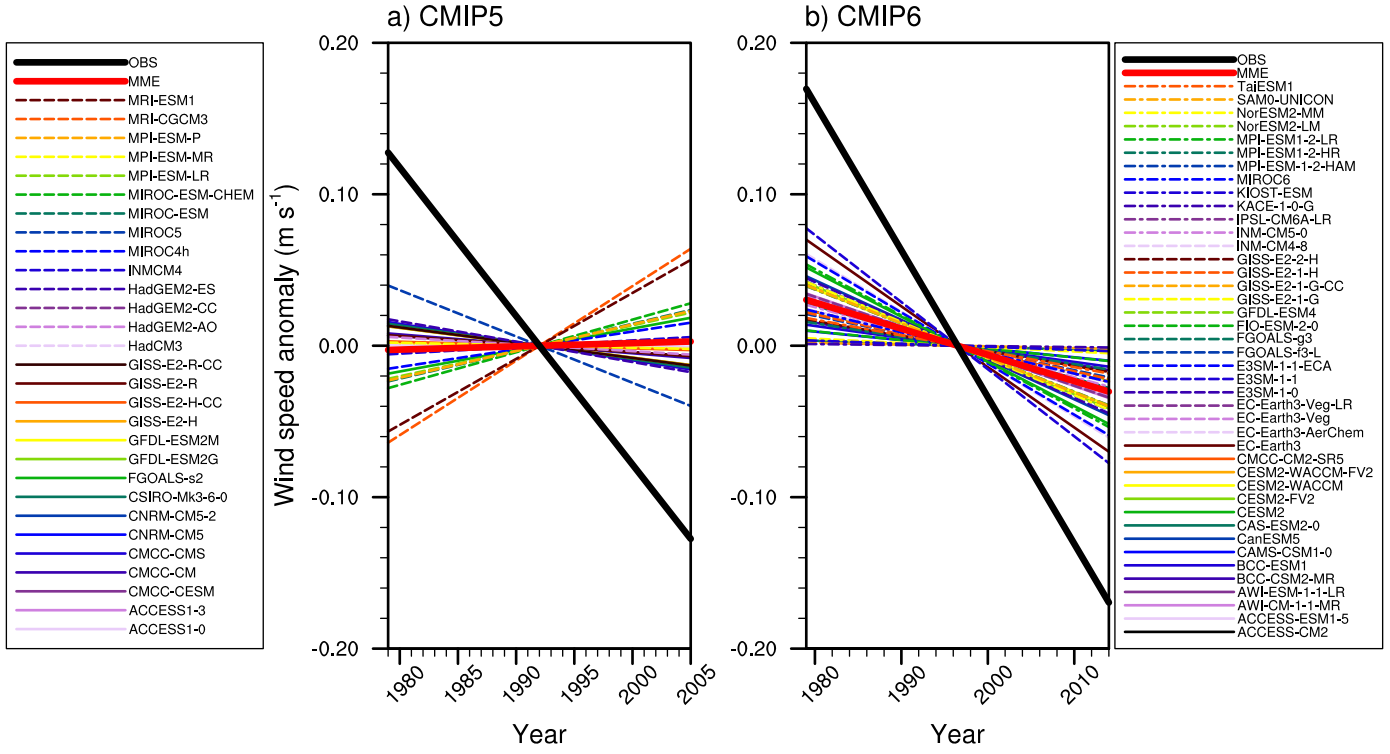

Fig. 3. Linear trends of surface wind speed anomaly (ms^{-1}) for (a) CMIP5 GCMs and (b) CMIP6 GCMs, together with the observations and MMEs averaged over all the stations. The reference periods to compute wind speed anomalies are 1979–2005 for CMIP5 and 1979–2014 for CMIP6.

The CMIP5 MME also shows a slight increasing trend, indicating that the CMIP5 models perform poorly in reproducing the observed wind speed trend. Conversely, the CMIP6 GCMs exhibit high simulation skills for annual wind speed evolution. All CMIP6 models can reproduce a 35-year decline in wind speed, of which E3SM-1-1 has the greatest reduction of 0.16 ms^{-1} during 1979–2014. Nevertheless, the CMIP6 GCMs generally underestimate the magnitude of wind speed variation, and the total drop in CMIP6 MME is only 0.06 ms^{-1}.

For the annual cycle of wind speed in Fig. 4, the observed wind speed varies relatively flatly, fluctuating between 3.4 and 3.8 ms^{-1}, with the largest wind speed value in April and the smallest in December and January. The most striking difference of simulated wind speed comparing with observation is that the wind speed is larger in winter and smaller in summer. From the MME, the simulated wind speed generally reaches its maximum in January and minimum in August. In the CMIP5 models, HadGEM2-ES and HadGEM2-CC can roughly

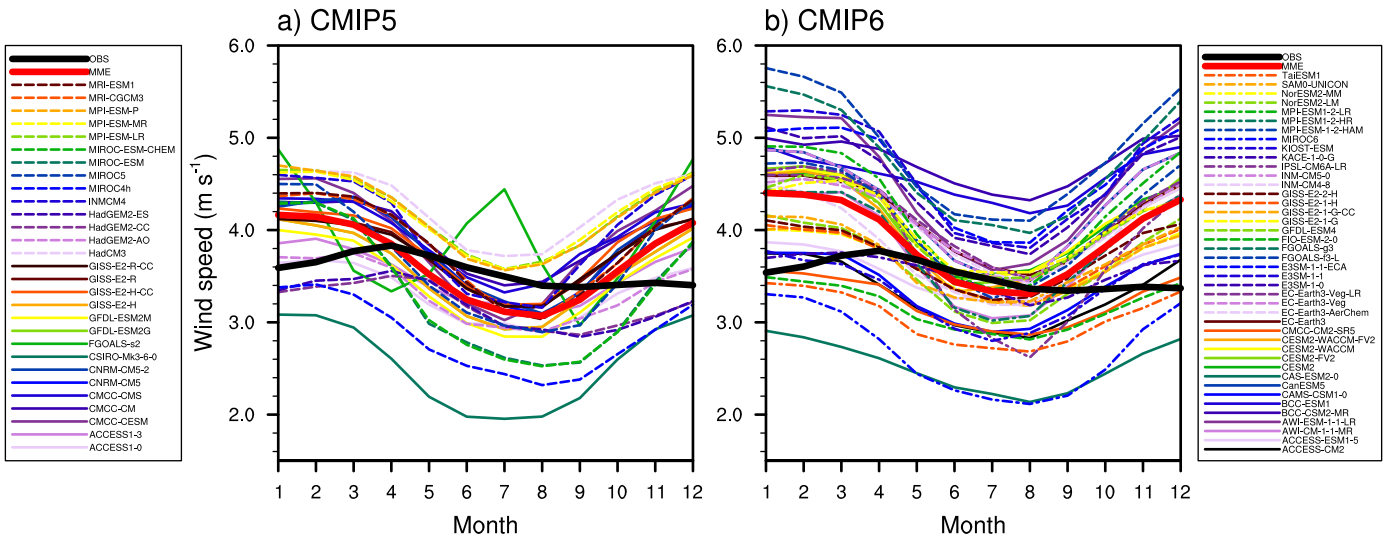

Fig. 4. Monthly surface wind speeds (ms^{-1}) of (a) CMIP5 GCMs and (b) CMIP6 GCMs, together with the observed speeds and MMEs averaged over all the stations for the period of 1979–2005 and the period of 1979–2014, respectively.

simulate the intra-annual variation characteristics of wind speed. Interestingly, FGOALS-s2 exhibits strong fluctuations, implying it has the worst simulation. The CMIP6 models exhibit intra-annual variability characteristics consistent with the CMIP5, leading to a general underestimate of wind speed from May to August and an overestimate from September to April in almost all the models.

Fig. 5 shows the standard deviation of wind speed for two different periods of the observations, CMIP5 and CMIP6 MMEs, and their respective discrepancies from the observations. It is found that the wind speed shows the highest variability over Europe, central Asia, South Asia, and Southeast Asia with values above 0.4 in the observations (Fig. 5a and b). Models generally underestimate wind speed variability, with a highest value of 0.2; and the discrepancy between CMIP5 and CMIP6 models is negligible. The above results can be summarized as follows: the CMIP6 models have shown considerable progress compared to the CMIP5; and they are more consistent with the observations. Next, we evaluate the wind speed over the three major wind power markets containing Europe, Asia, and North America based on the CMIP6 models only.

4. Regional assessment of surface wind speed in CMIP6

Fig. 6 shows the discrepancies of wind speed between GCMs and observations have obvious regional characteristics. For the whole

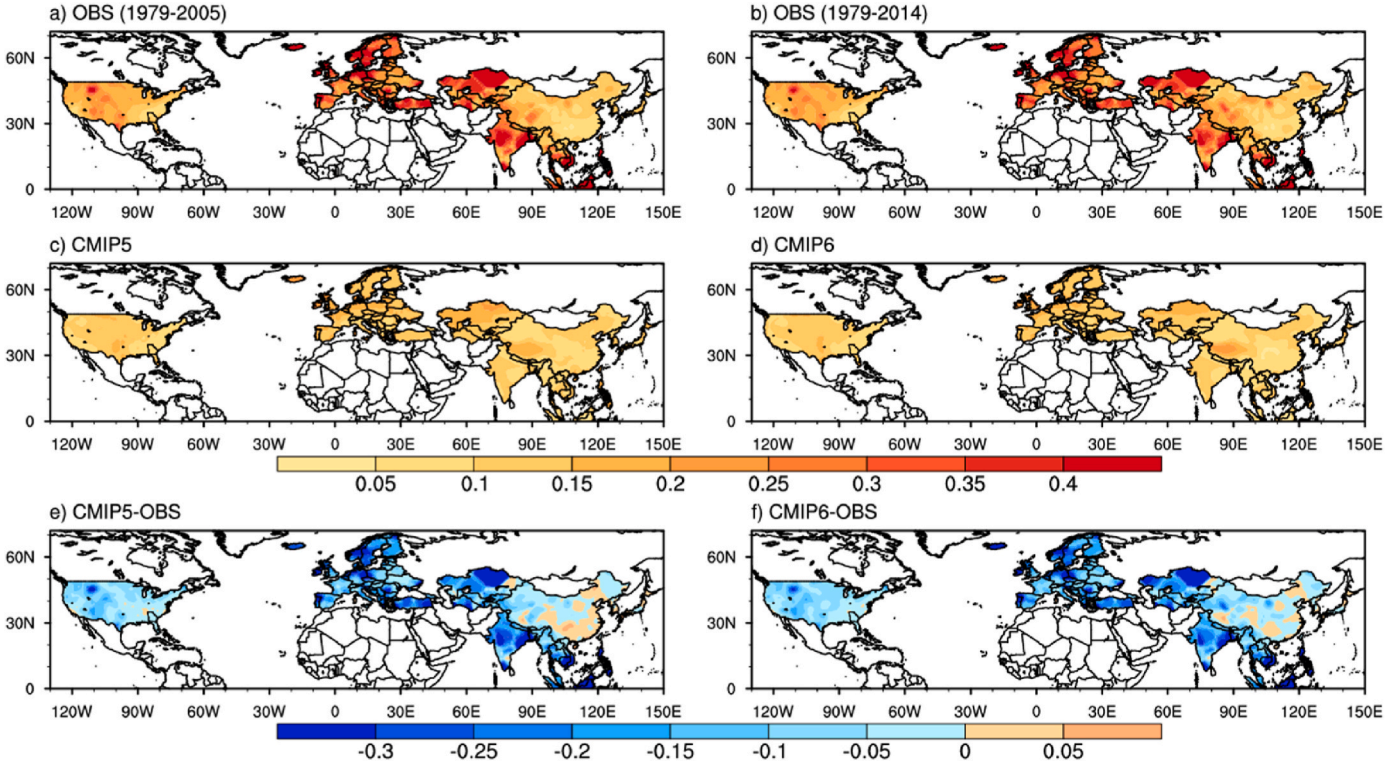

Fig. 5. Inter-annual standard deviation in surface wind speed for the observations during 1979–2005 (a) and during 1979–2014 (b), CMIP5 and CMIP6 MMEs (c and d), and the biases between CMIP5/CMIP6 and observations (e/f).

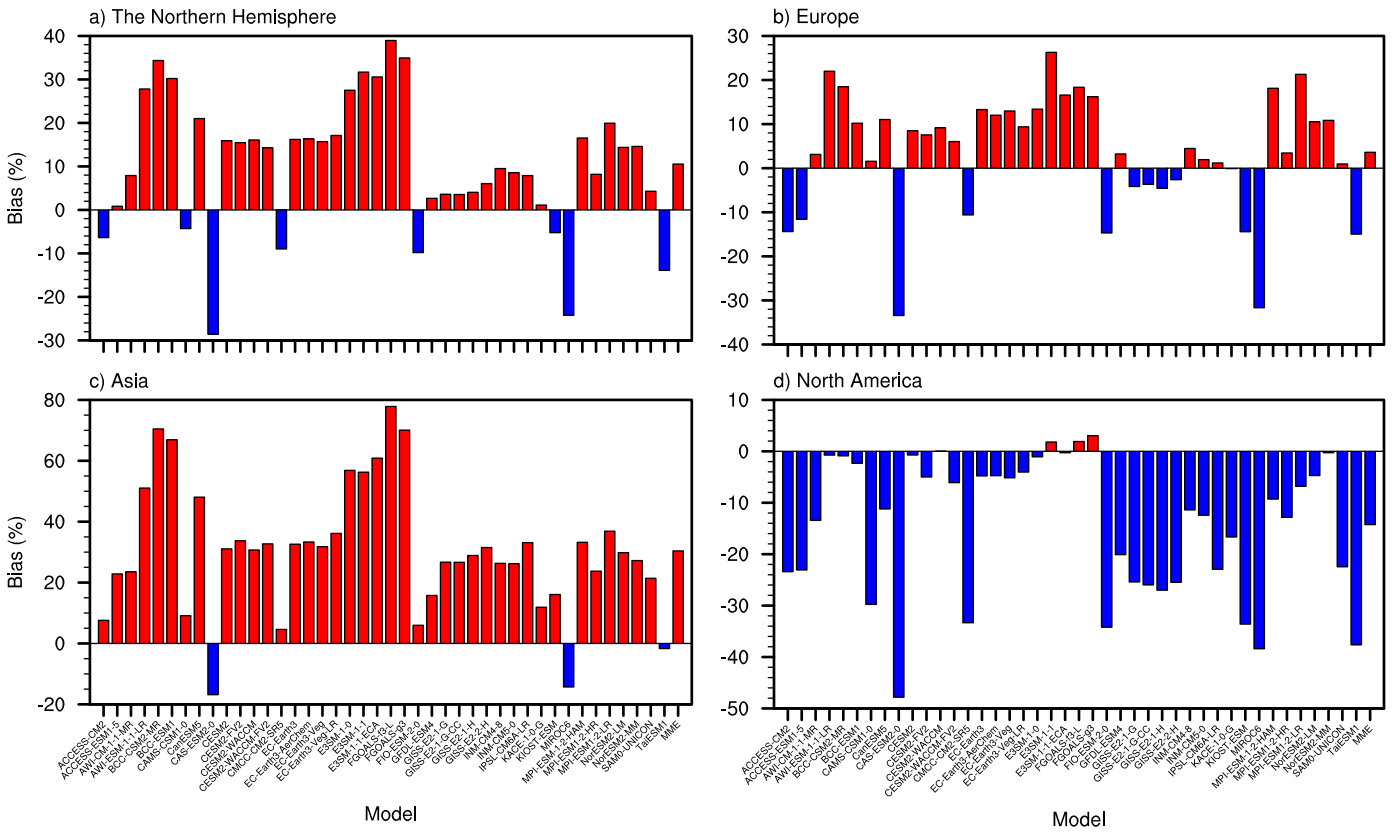

Fig. 6. Regional annual mean wind speed percentage biases over (a) the Northern Hemisphere, (b) Europe, (c) Asia, and (d) North America for the period of 1979–2014 derived from the CMIP6 models and MMEs compared with the observations.

Northern Hemisphere region, only eight out of the 42 models underestimate wind speed, and there is a positive bias of 10.5% for the MME. For the European territories, 29 and 13 models show positive and negative deviations, respectively, resulting in a slight overestimated MME of 3.6%. The simulations of the GCMs in Asia and North America show stark contrast, with the majority of the models (39 out of the 42) overestimating the wind speed in Asia while the same number of the models underestimating the wind speed in North America. The magnitude of the bias is smaller in North America, with an MME of −14.3%, while this bias is 30.4% in Asia. The large, overestimated wind speeds in Asia contribute to an overall positive bias of estimated wind speed in the Northern Hemisphere since there are more stations in Asia. We should still note that no single model can perform well in all regions, which is in accordance with Krishnan's [21] conclusion.

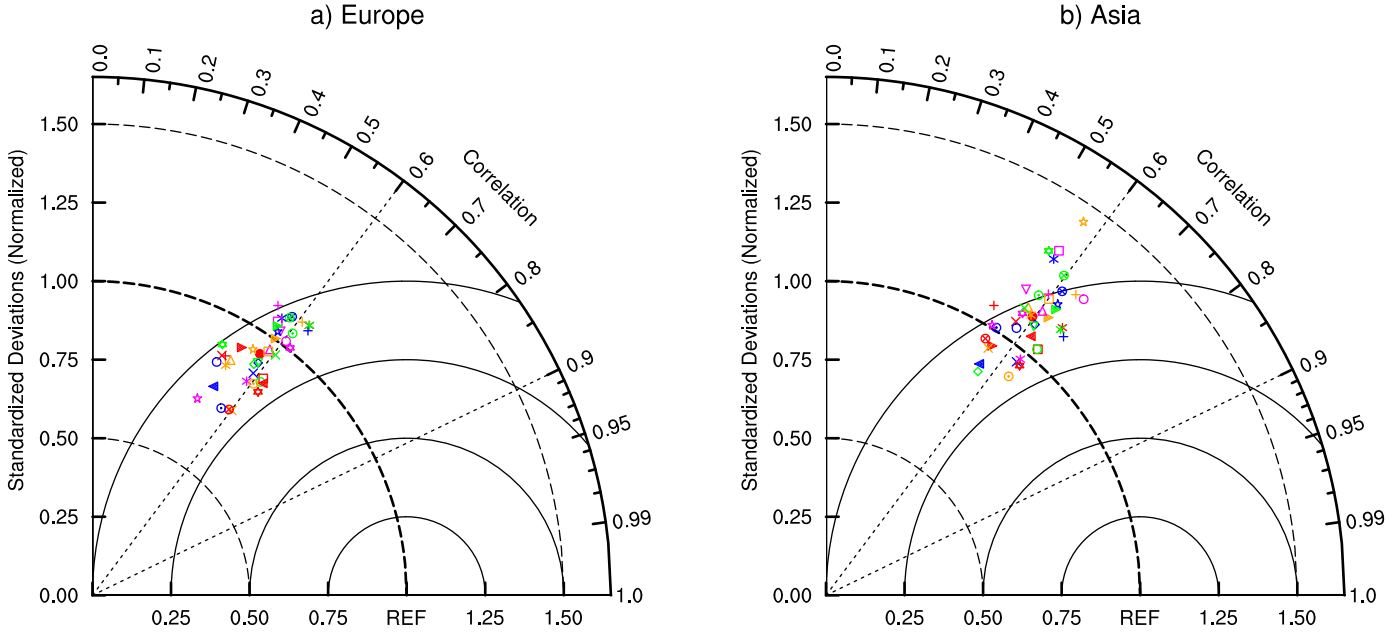

Fig. 7. Taylor diagrams of surface wind speed (ms^{-1}) over (a) Europe, (b) Asia and (c) North America for the CMIP6 models, together with their MMEs.

The 42 CMIP6 models have high consistency in Europe and Asia while showing large discrepancy in North America (Fig. 7). The standard deviation ratio, correlation coefficient, and root mean square difference of the MMEs are 0.94, 0.57, and 0.90 in Europe and 1.10, 0.60, and 0.96 in Asia, implying slightly better correlation and larger spatial variability in simulating wind speed in Asia. Relatively poor simulations of the GCMs are observed in North America, and more dispersed distribution of the models imply stronger inconsistency. In particular, the range of correlation coefficient spreads to 0.12–0.72, with standard deviation ratio, correlation coefficient, and root mean square difference of 1.13, 0.45, and 1.12 in MME. Several factors may lead to bias in the simulation of wind speed over North America. Climate models generally fail to represent diurnal differences in North American surface wind speeds because they fail to capture changes in atmospheric turbulence at night, and they cannot correctly simulate the nighttime boundary layer, especially the changes of surface flux under stable conditions. In addition, the sensitivity of climate models to underlying surface types is uneven in North America, with many models showing little sensitivity to surface types like forest and open water, which may introduce bias in the simulation of wind speed over North America [42].

The trends of wind speed in different regions in the CMIP6 models are presented in Fig. 8. All regions show strong decreases in wind speed during 1979–2014, with the largest total decline occurring in Europe at a value of 0.43 ms^{-1}. Almost all the models can reproduce the downward trend of each region. In Europe, E3SM-1-1 has the closest trend with the observed data, with a value of 0.28 ms^{-1}. In Asia, although most GCMs can generally simulate the decreasing trend of wind speed, their magnitudes are much smaller than the observed. The wind speed drop in North America is the smallest among the three regions, at 0.26 ms^{-1}; and the trends of the GCMs in this region are much closer to the observations.

For shorter time scales, the simulated monthly wind speed in each region also reaches a minimum in the warm season and a maximum in the cold season (Fig. 9). From the observations, the annual cycle in Asia is quite similar to that in the Northern Hemisphere as a whole (Fig. 3b), peaking in April and reaching its lowest wind speeds in December, and January. This finding corroborates the assessment of Liu et al. [43] for the wind power density in China, since the Chinese stations occupy the majority of Asia. In Europe and North America, the annual cycle of wind speed is not clearly characterized, and the regional-level results reinforce the lack of capability of the GCMs to accurately reproduce intra-annual variability in wind speed.

5. Projected changes of surface wind speed and wind power density

To analyze the future changes in surface wind speed and wind energy resources, we use MMEs of the CMIP6 projections of monthly wind speed under four different scenarios, i.e., SSP1-2.6, SSP2-4.5, SSP3-7.0, and SSP5-8.5. First, the time series and trends of wind speed for the historical and four future scenarios over 1965–2099 in the Northern Hemisphere and three regions are shown in Fig. 10. In general, wind speeds will continue the historical downward trend under all four scenarios, decreasing more rapidly under the higher emission scenarios. However, in all regions except North America, the wind speed decline most sharply under the SSP3-7.0 scenario, rather than under the highest emissions of SSP5-8.5. This feature is most pronounced in Asia, where wind speeds decline most severely under SSP3-7.0, even exceeding the magnitude of the historical period (Fig. 10c). In North America, however, SSP2-4.5 and SSP5-8.5 are the two scenarios with the fastest decreasing wind speeds (Fig. 10d). Interestingly, in all regions, wind speeds show an evidently positive trend in the lowest emission scenario of SSP1-2.6, starting in the 2070s. This is consistent with the fact that the GHG emission in SSP1-2.6 has reduced substantially during the end of the 21st century and may be favorable for the recovery of wind speed.

Fig. 11 shows the time series and trends of wind power density at 80-m, and the result is similar to that in Fig. 10. The decreasing trend of wind power density in the future is generally weaker than that in the historical period. In all regions, the wind power density trends are similar under the SSP1-2.6 and SSP2-4.5 scenarios, and the decreasing trends are relatively slow. In the Northern Hemisphere, the reductions of wind power density under the SSP3-7.0 and SSP5-8.5 scenarios are significantly greater than those under the two lower emission scenarios. In North America, wind power density decreases most sharply at SSP5-8.5 and most gently at SSP3-7.0, while in other regions, it decreases most significantly at SSP3-7.0, followed by SSP5-8.5.

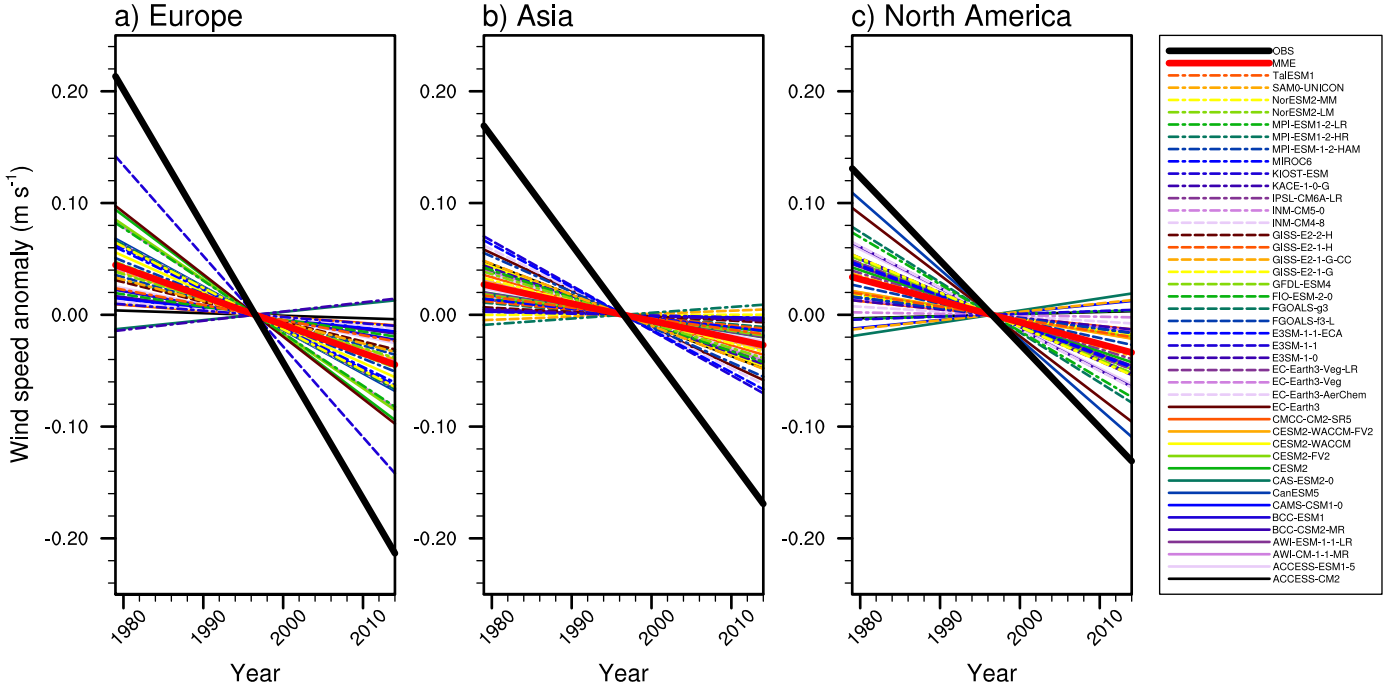

Fig. 8. Same as the right panel of Fig. 3, but for different regions and their MMEs.

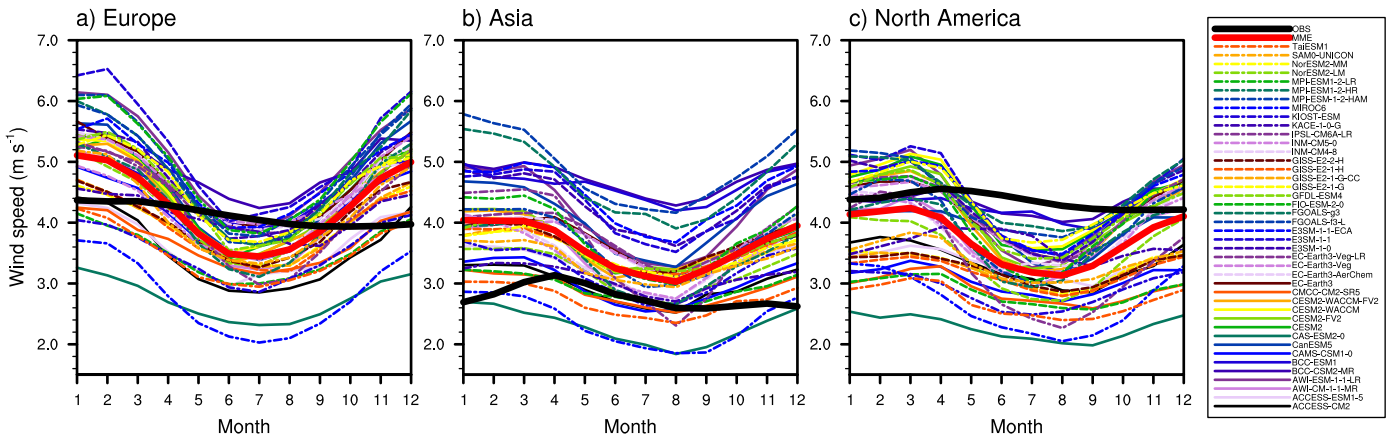

Fig. 9. Same as the right panel of Fig. 4, but for different regions and their MMEs.

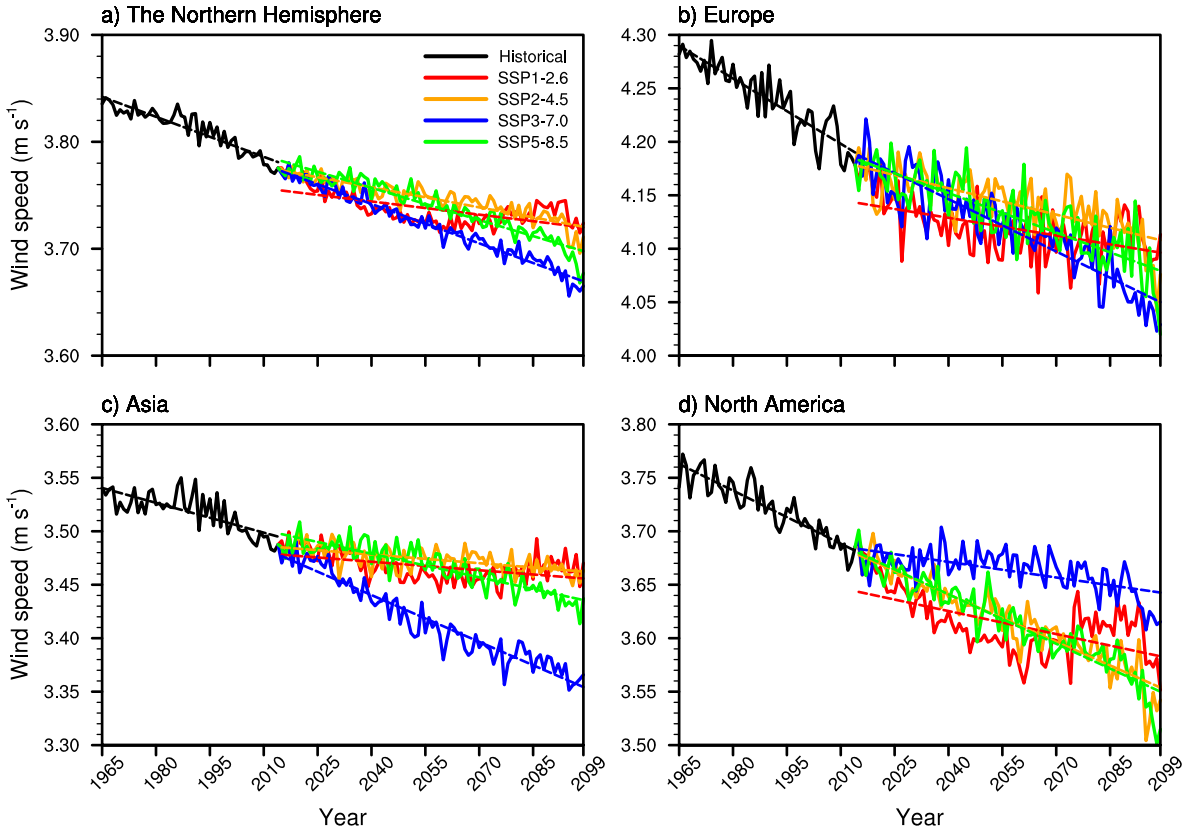

Fig. 10. Evolution and linear trends of historical and projected surface wind speed (ms^{-1}) under different scenarios over (a) the Northern Hemisphere, (b) Europe, (c) Asia, and (d) North America. The black, red, orange, blue, and green lines represent historical period, SSP1-2.6, SSP2-4.5, SSP3-7.0, and SSP5-8.5 scenarios, respectively.

Fig. 12 displays the spatial pattern of wind speed trend over the future period (2050–2099) relative to the historical period (1965–2014) in different regions and scenarios. The crossed areas in Fig. 12 show the region where at least 82.6% of the models (19 out of the 23 CMIP6 GCMs) have the same trend sign. For the lower emission scenarios of SSP1-2.6 and SSP2-4.5, the uncertainty of the models is large and the significance of the wind speed trend is not high, showing negative trends mainly in the eastern US, western and northeast China. Europe only shows a significant decreasing trend under SSP3-7.0; and wind speeds over most of China also drop fastest under SSP3-7.0. However, under the higher emission scenario of SSP5-8.5, the decline in wind speed in China is merely in the western region. Notably, there are significant increases in Southeast Asia under four scenarios, presumably due to increased land-sea thermal differences caused by global warming, which leads to an enhanced Asia monsoon [44–47]. In the US, wind speeds decrease strongly under all scenarios, except in the southern region. However, under SSP3-7.0, there is a less-than-significant positive trend in wind speed in the eastern US, which contributes to the flattest trend in SSP3-7.0 in North America.

Projected changes in wind power density show a reduction over most of the Northern Hemisphere, in general agreement with the spatial distribution characteristics of the wind speed trend (Fig. 13). In Europe, the Iberian Peninsula, Apennine Peninsula and the UK display significant 10% wind power density reduction under all four scenarios. In

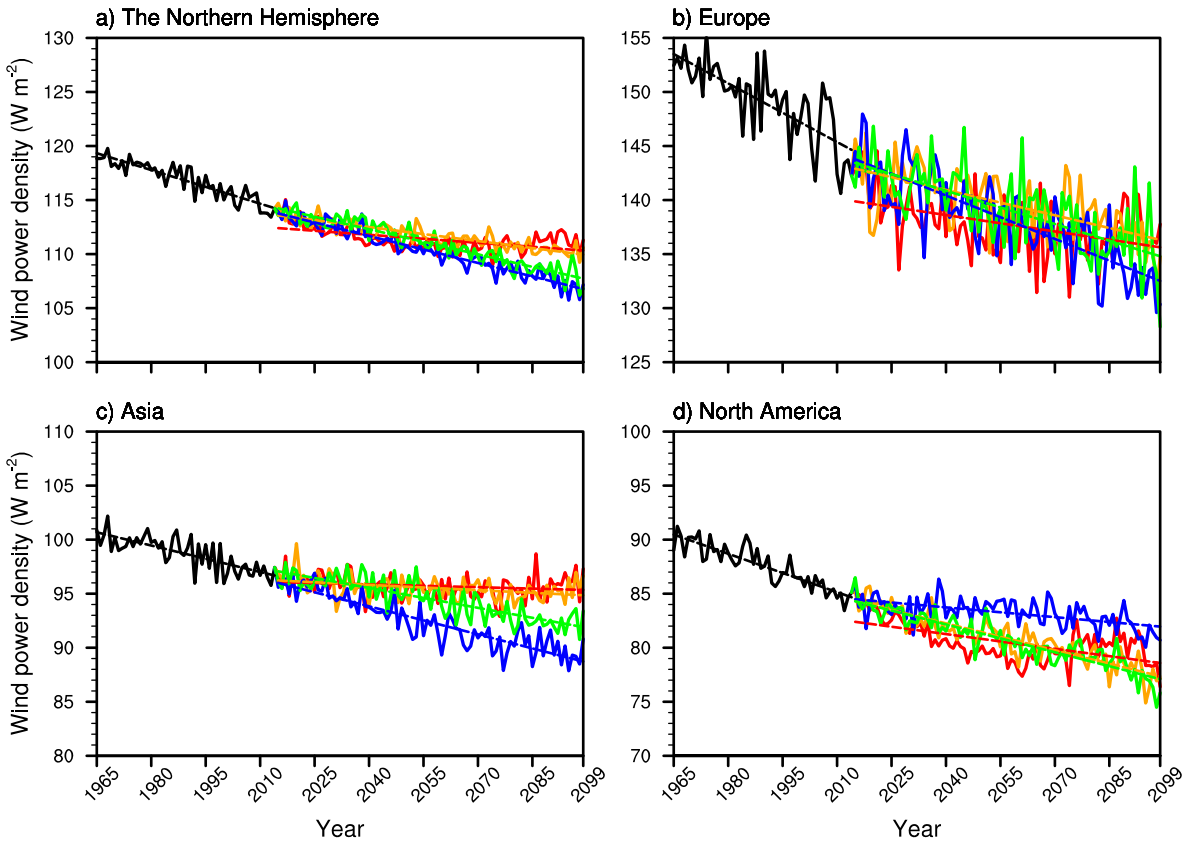

Fig. 11. Same as Fig. 10, but for wind power density (Wm^{-2}).

addition, central Europe has a considerable reduction under SSP3-7.0. In Asia, the largest reduction occurs under SSP3-7.0, covering the whole China with a 20% reduction; however, only the Tibetan Plateau region in China exhibits a significant reduction under the other scenarios. The opposite variation occurs in Southeast Asia, where more than 30% rise in wind power density is projected under SSP2-4.5. Most of North America shows a significant decrease in wind power density, with the eastern region exceeding the western region under both SSP1-2.6 and SSP2-4.5. There are generally 15% decreases under the two higher scenarios.

6. Discussion

In this study, it is worth noting that the model simulations of wind speed magnitudes and trends vary considerably across regions. For example, models generally have a negative bias in North America and a positive bias in Asia. Differences also exist between individual models, for example the change of surface wind speed from E3SM1-1 gets 0.16 ms^{-1}, while MIROC6 just gets less than 0.01 ms^{-1} (Fig. 3b) during 1979–2014. In addition, CAS-ESM1-0 underestimates the wind speed in all regions, while FGOALS-f3 has overestimations in all regions. Several studies have pointed out that model uncertainties for mean-state and variability simulations arise from several reasons, such as the difference of model setting, and the internal variability of the climate system [48–51], and the fact that the global climate models may not be able to perfectly assess the local scale wind patterns and especially those formed by local scale phenomena. For instance, in terms of the atmospheric component, GAMIL3 is adopted for FGOALS-g3, AGCM for MIROC6, and AM4.1 for GFDL-ESM4 [52–54]. The atmospheric component includes physical parameterizations such as cloud microphysics, turbulence, cumulus convection, radiation transfer and aerosol chemistry, and the different parameterization schemes may lead to differences in wind speed simulations. In addition, the potential change of the air density under global warming might introduce minor uncertainty on our estimation of the future projection of wind energy resources using CMIP models.

Regarding CMIP6 future projections, we find a non-linear relationship between GHG emission and wind energy change. Wind energy declines the fastest in Europe and Asia under the medium-high emission scenario of SSP3-7.0. In particular, wind speed in China decreases significantly in all regions under SSP3-7.0. The unique impact of the SSP3-7.0 scenario on climate in China has also been mentioned in previous research. Chen [30] showed that SSP3-7.0 represents the highest emissions of SO_2, N_2O, and CH_4 among the nine emission scenarios in the CMIP6, and thus leads to the most extensive climate change damages and negative economic impacts. Projections for future drought conditions in China under SSP3-7.0 are different to the other three scenarios (SSP1-2.6, SSP2-4.5,and SSP5-8.5). In addition, China's economy grows most slowly under SSP3-7.0 among four scenarios, due to the changes in the Earth's radiative balance and changes in the atmospheric circulation in this peculiar scenarios, leads to anomalous changes in precipitation and wind speed [55].

On the contrary, the decreasing trend of wind speed in North America is the smallest under SSP3-7.0, suggesting that the global wind energy map is sensitive to emission scenario. Further discussion of the dynamics of the nonlinear response of wind speed to GHG emission is beyond the purpose of this work, and will be investigated in the future.

7. Conclusions

This study performs an assessment of simulation skills relative to the observations using the GCMs of the CMIP5 and CMIP6 and also investigates the characteristics of wind speed and wind power density over the Northern Hemisphere under four emission scenarios of SSP1-2.6, SSP2-4.5, SSP3-7.0, and SSP5-8.5. Moreover, we analyze the evolution of wind resources in the three major wind markets of the Northern

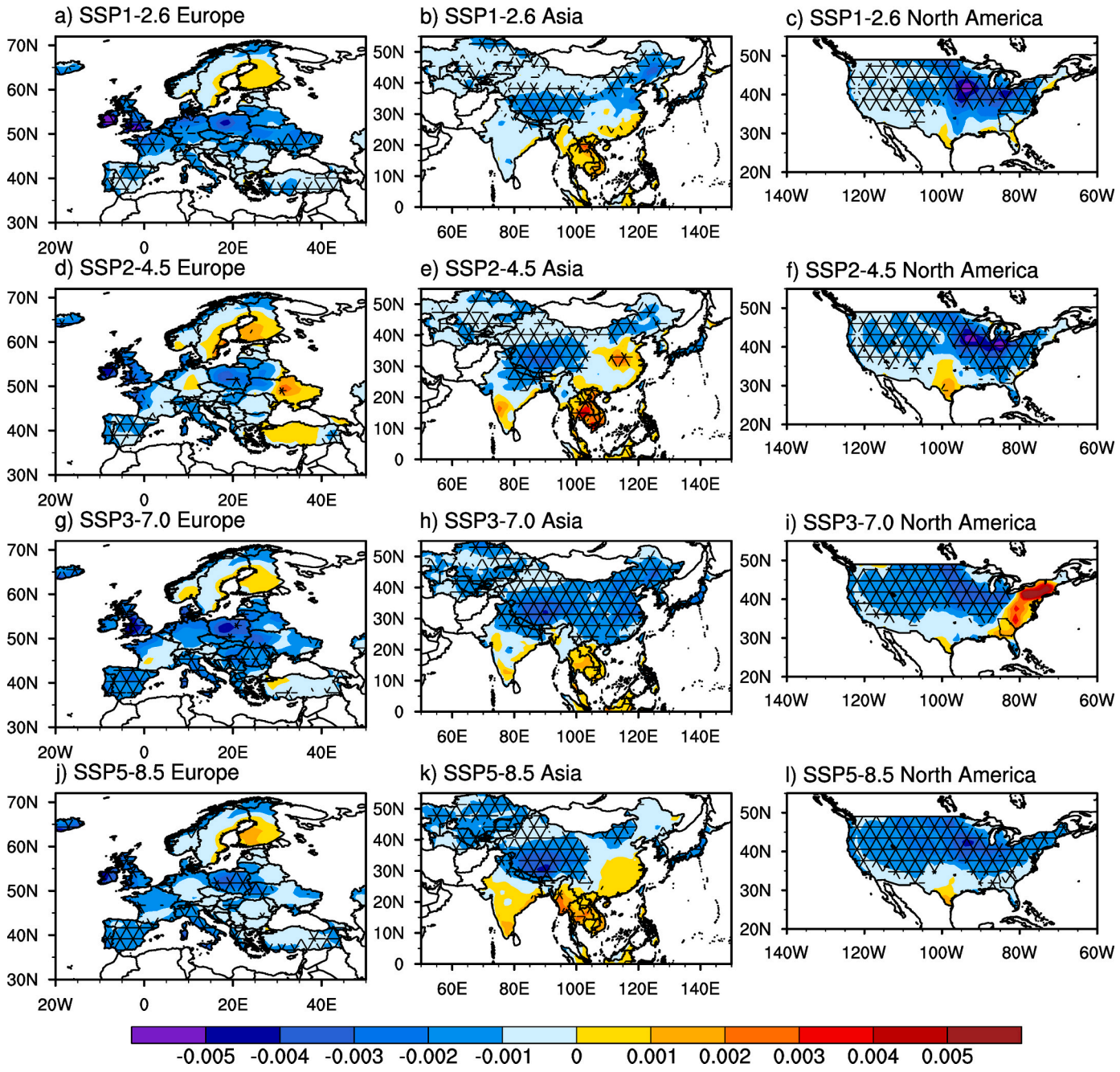

Fig. 12. Surface wind speed trends ($ms^{-1}year^{-1}$) for future (2050–2099) relative to the historical period (1965–2014) over Europe (a, d, g, and j), Asia (b, e, h, and k) and North America (c, f, i, and l) under SSP1-2.6 (a–c), SSP2-4.5 (d–f), SSP3-7.0 (g–i), and SSP5-8.5 (j–l). The crossed area indicates the region where more than 19 out of the 23 CMIP6 GCMs agree on the sign of the change.

Hemisphere, namely, Europe, Asia, and North America under the four emission scenarios. The most critical conclusions are summarized as follows.

In general, the CMIP6 models show better capability in simulating surface wind speed over the whole Northern Hemisphere in terms of pattern correlation coefficient, standard deviation ratio, and root-mean-square difference than the CMIP5 models; and the biases compared with observations reduce apparently in Europe and Asia. Despite underestimating the magnitude of the trend, all CMIP6 models reproduce decreasing trends in wind speed, while nearly half of the CMIP5 models show rising trends opposite to the observations. CESM2, CESM2-WACCM, EC-EARTH3, and NorESM2-MM are verified as the best-performing models of the CMIP6 family based on parameters involved in the Taylor diagram. However, the CMIP6 models display similarly poor capability as the CMIP5, failing to reproduce the intra-annual cycle and inter-annual standard deviations of wind speed.

The CMIP6 GCMs generally overestimate the wind speed in Asia and underestimate that in North America, with average values of 30.4% and −14.3% for Asia and North America, respectively. Taylor diagram demonstrates higher simulation skills and higher consistency of the CMIP6 GCMs in Europe and Asia than in North America. Wind speeds in all regions were decreasing over the period 1979–2014, with the largest drop of 0.43 ms^{-1} in Europe; and most models can similarly reproduce the decline in wind speed in all regions, yet still underestimate the magnitude, especially in Asia. Consistent with the results for the whole Northern Hemisphere, the simulated regional monthly wind speeds are all characterized by small values in summer and large values winter, which is not supported by the observations.

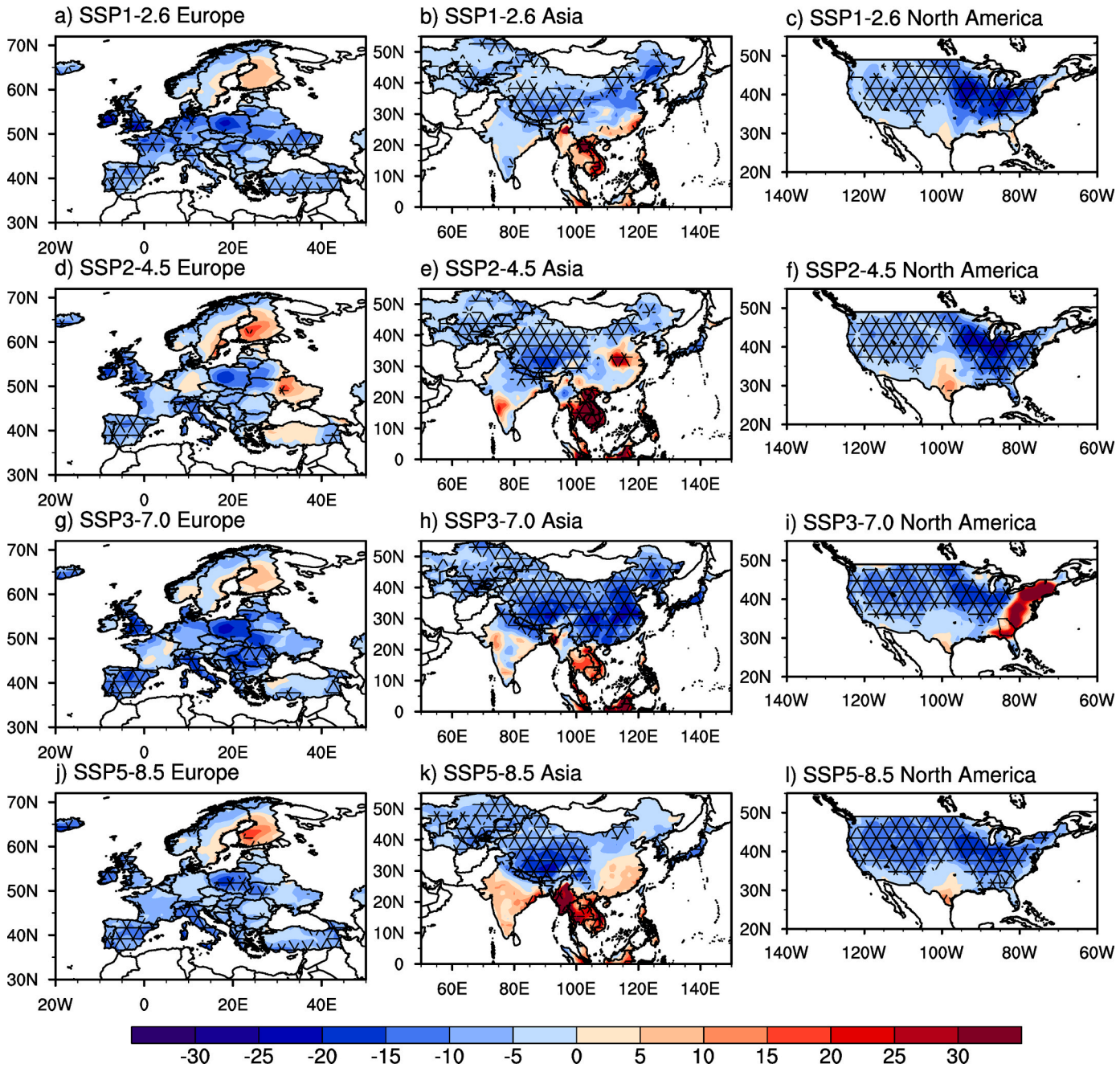

Fig. 13. Percentage changes in wind power density for future (2050–2099) relative to the historical period (1965–2014) over different regions under four scenarios. The definition of the crossed region is the same as that in Fig. 12.

Surface wind speeds will continue to decline in the future under all emission scenarios based on the CMIP6 projections. However, declining wind energy shows a non-linear relationship with GHG emissions. The largest surface wind speed and wind power density decline will appear in Europe and Asia under the SSP3-7.0 scenario, especially in Asia, which covers almost all regions of China, but the smallest drop will be in North America, suggesting a reshaped global wind energy map under this scenario. Despite the uniqueness of SSP3-7.0, our finding indicates the importance of reducing GHG emissions, which has an important role in mitigating the energy crisis and sustainable development of human society.

The advancements of the CMIP6 models over the CMIP5 noted in this study may be attributed to the progress in the parameterization of physical processes. However, the CMIP6 GCMs still have some limitations, due to coarse spatial resolution and inaccuracies in areas with complex topography. The estimate of possible processes in the evolution of wind resources under climate change is a crucial reference for the wind energy sector. Moreover, future wind energy projections need to be more carefully, e.g., by conducting smaller-scale studies in the regions for the application of more favorable wind power planning.

CRediT authorship contribution statement

Haozeyu Miao: Writing – original draft, Software, Validation, Formal analysis, Investigation. **Haiming Xu:** Supervision, Writing – review & editing. **Gang Huang:** Conceptualization, Supervision, Funding acquisition. **Kai Yang:** Methodology, Software, Writing – review & editing.

Declaration of competing interest

The authors declare that they have no known competing financial interests or personal relationships that could have appeared to influence the work reported in this paper.

Acknowledgements

Observational surface wind speeds in this study were obtained at https://www.ncdc.noaa.gov/isd supported by the National Centers for Environmental Information and at http://data.cma.cn/data/detail/dataCode/SURF_CLI_CHN_MUL_DAY_V3.0/keywords/v3.0.html from the China Meteorological Data Service Center. The CMIP5 and CMIP6 historical and projected surface wind speed data were downloaded from the website of the World Climate Research Programme at https://esgf-node.llnl.gov/search/cmip5 and https://esgf-node.llnl.gov/search/cmip6, respectively. This work was supported by the National Natural Science Foundation of China (42141019, 41831175, 91937302, and 41721004), STEP (2019QZKK0102).

References

[1] D. Saygin, R. Kempener, N. Wagner, et al., The implications for renewable energy innovation of doubling the share of renewables in the global energy mix between 2010 and 2030, Energies 8 (6) (2015) 5828–5865.
[2] C.W. Zheng, C.Y. Li, J. Pan, et al., An overview of global ocean wind energy resource evaluations, Renew. Sustain. Energy Rev. 53 (2016) 1240–1251.
[3] Global Wind Energy Council, GWEC| Global Wind Report 2021, 2021.
[4] J.F. Manwell, J.G. McGowan, A.L. Rogers, Wind Energy Explained: Theory, Design and application[M], John Wiley & Sons, 2010.
[5] Q. Tian, G. Huang, K. Hu, et al., Observed and global climate model based changes in wind power potential over the Northern Hemisphere during 1979-2016, Energy 167 (2019) 1224–1235.
[6] S.C. Pryor, J. Ledolter, Addendum to "Wind speed trends over the contiguous United States", J. Geophys. Res. Atmos. 115 (D10) (2010).
[7] H. Guo, M. Xu, Q. Hu, Changes in near-surface wind speed in China: 1969-2005, Int. J. Climatol. 31 (3) (2011) 349–358.
[8] C. Azorin-Molina, S.M. Vicente-Serrano, T.R. McVicar, et al., Homogenization and assessment of observed near-surface wind speed trends over Spain and Portugal, 1961-2011, J. Clim. 27 (10) (2014) 3692–3712.
[9] T.R. McVicar, T.G. Van Niel, L.T. Li, et al., Wind speed climatology and trends for Australia, 1975-2006: capturing the stilling phenomenon and comparison with near-surface reanalysis output, Geophys. Res. Lett. 35 (20) (2008).
[10] H. Wan, X.L. Wang, V.R. Swail, Homogenization and trend analysis of Canadian near-surface wind speeds, J. Clim. 23 (5) (2010) 1209–1225.
[11] S.C. Pryor, R.J. Barthelmie, Climate change impacts on wind energy: a review, Renew. Sustain. Energy Rev. 14 (1) (2010) 430–437.
[12] K.E. Taylor, R.J. Stouffer, G.A. Meehl, An overview of CMIP5 and the experiment design, Bull. Am. Meteorol. Soc. 93 (4) (2012) 485–498.
[13] J. Zha, J. Wu, D. Zhao, et al., Future projections of the near-surface wind speed over eastern China based on CMIP5 datasets, Clim. Dynam. 54 (3) (2020) 2361–2385.
[14] K. Ruosteenoja, T. Vihma, A. Venäläinen, Projected changes in European and North Atlantic seasonal wind climate derived from CMIP5 simulations, J. Clim. 32 (19) (2019) 6467–6490.
[15] M. Dobrynin, J. Murawsky, S. Yang, Evolution of the global wind wave climate in CMIP5 experiments, Geophys. Res. Lett. 39 (18) (2012).
[16] D. Carvalho, A. Rocha, M. Gómez-Gesteira, et al., Potential impacts of climate change on European wind energy resource under the CMIP5 future climate projections, Renew. Energy 101 (2017) 29–40.
[17] A.T. Abolude, W. Zhou, A.A. Akinsanola, Evaluation and projections of wind power resources over China for the energy industry using CMIP5 models, Energies 13 (10) (2020) 2417.
[18] S. Mohan, P.K. Bhaskaran, Evaluation of CMIP5 climate model projections for surface wind speed over the Indian Ocean region, Clim. Dynam. 53 (9) (2019) 5415–5435.
[19] V. Eyring, S. Bony, G.A. Meehl, et al., Overview of the coupled model Intercomparison Project phase 6 (CMIP6) experimental design and organization, Geosci. Model Dev. (GMD) 9 (5) (2016) 1937–1958.
[20] R.J. Stouffer, V. Eyring, G.A. Meehl, et al., CMIP5 scientific gaps and recommendations for CMIP6, Bull. Am. Meteorol. Soc. 98 (1) (2017).
[21] A. Krishnan, P.K. Bhaskaran, Skill assessment of global climate model wind speed from CMIP5 and CMIP6 and evaluation of projections for the Bay of Bengal, Clim. Dynam. 55 (9) (2020) 2667–2687.
[22] T. Oudar, J. Cattiaux, H. Douville, Drivers of the northern extratropical eddy-driven jet change in CMIP5 and CMIP6 models, Geophys. Res. Lett. 47 (8) (2020), e2019GL086695.
[23] S. Zhang, X. Li, Future projections of offshore wind energy resources in China using CMIP6 simulations and a deep learning-based downscaling method, Energy 217 (2021), 119321.
[24] D. Carvalho, A. Rocha, X. Costoya, et al., Wind energy resource over Europe under CMIP6 future climate projections: what changes from CMIP5 to CMIP6, Renew. Sustain. Energy Rev. 151 (2021), 111594.
[25] M.J. Gidden, K. Riahi, S.J. Smith, et al., Global emissions pathways under different socioeconomic scenarios for use in CMIP6: a dataset of harmonized emissions trajectories through the end of the century, Geosci. Model Dev. (GMD) 12 (4) (2019) 1443–1475.
[26] H. Schandl, Y. Lu, N. Che, et al., Shared socio-economic pathways and their implications for global materials use, Resour. Conserv. Recycl. 160 (2020), 104866.
[27] J. Wu, Y. Shi, Y. Xu, Evaluation and projection of surface wind speed over China based on CMIP6 GCMs, J. Geophys. Res. Atmos. 125 (22) (2020), e2020JD033611.
[28] A. Martinez, G. Iglesias, Wind resource evolution in Europe under different scenarios of climate change characterised by the novel Shared Socioeconomic Pathways, Energy Convers. Manag. 234 (2021), 113961.
[29] A. Martinez, G. Iglesias, Climate change impacts on wind energy resources in North America based on the CMIP6 projections, Sci. Total Environ. 806 (2022), 150580.
[30] Y. Chen, A. Liu, X. Cheng, Quantifying economic impacts of climate change under nine future emission scenarios within CMIP6, Sci. Total Environ. 703 (2020), 134950.
[31] A. Smith, N. Lott, R. Vose, The integrated surface database: recent developments and partnerships, Bull. Am. Meteorol. Soc. 92 (6) (2011) 704–708.
[32] H. Miao, D. Dong, G. Huang, et al., Evaluation of Northern Hemisphere surface wind speed and wind power density in multiple reanalysis datasets, Energy 200 (2020), 117382.
[33] Z. Zeng, A.D. Ziegler, T. Searchinger, et al., A reversal in global terrestrial stilling and its implications for wind energy production, Nat. Clim. Change 9 (12) (2019) 979–985.
[34] R. Kvasov, S. Cruz-Pol, J. Colom-Ustáriz, et al., Weather radar data visualization using first-order interpolation, in: 2013 IEEE International Geoscience and Remote Sensing Symposium-IGARSS, IEEE, 2013, pp. 3574–3577.
[35] G.P. Cressman, An operational objective analysis system, Mon. Weather Rev. 87 (10) (1959) 367–374.
[36] K.E. Taylor, Summarizing multiple aspects of model performance in a single diagram, J. Geophys. Res. Atmos. 106 (D7) (2001) 7183–7192.
[37] E.W. Peterson, J.P. Hennessey Jr., On the use of power laws for estimates of wind power potential, J. Appl. Meteorol. Climatol. 17 (3) (1978) 390–394.
[38] J. Wang, J. Hu, K. Ma, Wind speed probability distribution estimation and wind energy assessment, Renew. Sustain. Energy Rev. 60 (2016) 881–899.
[39] M.R. Islam, R. Saidur, N.A. Rahim, Assessment of wind energy potentiality at Kudat and Labuan, Malaysia using Weibull distribution function, Energy 36 (2) (2011) 985–992.
[40] J.S. Touma, Dependence of the wind profile power law on stability for various locations, J. Air Pollut. Control Assoc. 27 (9) (1977) 863–866.
[41] H. Sun, X. Gao, H. Yang, Experimental study on wind speeds in a complex-terrain wind farm and analysis of wake effects, Appl. Energy 272 (2020), 115215.
[42] Y. He, A.H. Monahan, C.G. Jones, et al., Probability distributions of land surface wind speeds over North America, J. Geophys. Res. Atmos. 115 (D4) (2010).
[43] F. Liu, F. Sun, W. Liu, et al., On wind speed pattern and energy potential in China, Appl. Energy 236 (2019) 867–876.
[44] G.A. Meehl, W.M. Washington, South Asian summer monsoon variability in a model with doubled atmospheric carbon dioxide concentration, Science 260 (5111) (1993) 1101–1104.
[45] A. Kitoh, S. Yukimoto, A. Noda, et al., Simulated changes in the Asian summer monsoon at times of increased atmospheric CO2, Journal of the Meteorological Society of Japan. Ser. II 75 (6) (1997) 1019–1031.
[46] Z.Z. Hu, M. Latif, E. Roeckner, et al., Intensified Asian summer monsoon and its variability in a coupled model forced by increasing greenhouse gas concentrations, Geophys. Res. Lett. 27 (17) (2000) 2681–2684.
[47] H. Ueda, A. Iwai, K. Kuwako, et al., Impact of anthropogenic forcing on the Asian summer monsoon as simulated by eight GCMs, Geophys. Res. Lett. 33 (6) (2006).
[48] M.D. Zelinka, T.A. Myers, D.T. McCoy, et al., Causes of higher climate sensitivity in CMIP6 models, Geophys. Res. Lett. 47 (1) (2020), e2019GL085782.
[49] F. Lehner, C. Deser, N. Maher, et al., Partitioning climate projection uncertainty with multiple large ensembles and CMIP5/6, Earth System Dynamics 11 (2) (2020) 491–508.
[50] R. Knutti, J. Sedláček, Robustness and uncertainties in the new CMIP5 climate model projections, Nat. Clim. Change 3 (4) (2013) 369–373.
[51] E. Veronika, B. Sandrine, G.A. Meehl, et al., Overview of the Coupled Model Intercomparison Project Phase 6 (CMIP6) Experimental Design and Organization, Geoscientific Model Development, 2016.
[52] L. Li, Y. Yu, Y. Tang, et al., The flexible global ocean-atmosphere-land system model grid-point version 3 (fgoals-g3): description and evaluation, J. Adv. Model. Earth Syst. 12 (9) (2020), e2019MS002012.
[53] H. Tatebe, T. Ogura, T. Nitta, et al., Description and basic evaluation of simulated mean state, internal variability, and climate sensitivity in MIROC6, Geosci. Model Dev. (GMD) 12 (7) (2019) 2727–2765.
[54] J.P. Dunne, L.W. Horowitz, A.J. Adcroft, et al., The GFDL Earth System Model version 4.1 (GFDL-ESM 4.1): overall coupled model description and simulation characteristics, J. Adv. Model. Earth Syst. 12 (11) (2020), e2019MS002015.
[55] D.T. Shindell, G.A. Schmidt, Southern Hemisphere climate response to ozone changes and greenhouse gas increases, Geophys. Res. Lett. 31 (18) (2004).